Study on Compressive Damage of Polymer Bonded Explosives by In-situ Micro Computed Tomography and Digital Volume Correlation Method †

Bin Dai [1],*, Chen Liu [1], Panpan Xu[1], Hua Chen [1]

[1] Institute of Chemical Materials, Chinese Academy of Engineering Physics, Mianyang, China
Emails: marsbear@163.com. Liuchen@caep.cn. PanpanXu@sina.com Chenhua@caep.cn

* Correspondence: marsbear@163.com; Tel.: +86 13508102781

† Presented at 18th International Conference on Experimental Mechanics (ICEM18), Brussels 1-5 July 2018.

Abstract: To study the three-dimensional (3D) morphological evolution of damage of the polymer bonded explosive (PBX) during compression process, the damage process of the PBX at the mesoscopic scale was analyzed. Furthermore, the damage evolution of the PBX was also deduced. The 3D deformation behavior and devolution of the internal microstructure of PBX during the in situ compression process were systematically investigated by integrating micro computed tomography (CT) imaging and digital volume correlation (DVC) method. The displacement and strain inside the PBX during the loading of down load were obtained through the DVC method. The results revealed that the strain concentration always appeared at binders between the granules before failure and led to granule internal cracking or granule edge cracking. The results further indicated that integration of micro CT and DVC technique can provide a more practical and effective method for investigating the structural features, strain, and damage mechanism of PBXs during compression process. This study has significant meaning for comprehensive investigation of the damage mechanical behavior of PBX.

Keywords: Polymer bonded explosive;Micro X-ray tomography;Digital volume correlation;In-situ compression

1. Introduction

Polymer bonded explosives (PBXs) are multi-phase composite materials constituted of thermoplastic polymeric binder and single-compound explosive crystals. This constitution determines the heterogeneity of their structure and discontinuity of their physical and mechanical properties [1]. Under packaging, transport, and other normal service conditions, explosives get subjected to a variety of vibration sources, impact, shock, and other similar events. Under these attack conditions, they bear loads of a relatively high loading rate; and under accident conditions, these PBXs may also experience drop, impact, etc. In these processes, explosives may undergo the generation of some structural defects and damages, which result in reduced strength and stiffness. Moreover, they experience further growth and polymerization under loads, temperature, and other actions, which ultimately leads to structural failure [2,3]. To quantify crack-related damages and the deformation localization and geometrical morphology incurred by them, scholars around the world have used scanning electron microscopy [4–7], acoustic emission, ultrasonic wave, digital image correlation (DIC) [8–12], and other methods to analyze the crack propagation and failure process of PBXs. However, for heterogeneous anisotropic materials such as PBXs, surface observation alone is incapable of either comprehensively reflecting the heterogeneity of internal deformation, or effectively obtaining the volume information of damage propagation (which exactly constitutes the primary means of damage propagation for materials). Some scholars [13] have tried to embed strain

indicators inside PBX in the packaging process and thus conducted an experimental study on the internal strain and stress states of explosives.

With the development of CT technique, micro CT can help in obtaining internal 3D structural images of the objects. This provides an effective method for obtaining the image for measuring the internal 3D deformation and strain field of the object. In 1999, Bay et al. [14] expanded the 2D digital images correlation method to the measurement of internal 3D displacement field and strain field of the substance, and proposed the DVC method. They measured the internal 3D displacement field of the cancellous bone under load, and calculated the 3D strain field through numerical differentiation calculation. Nonetheless, limited by resolution, CT images can only display cracks at CT resolution scale, but cannot reveal the generation and development of deformation localization before the formation of cracks at CT resolution scale. In this study, a CT-matched loading device was adopted to conduct the uniaxial compression of the explosive sample, and in-situ scanning was performed in stages. The obtained three-dimensional (3D) CT volume data were used to analyze the internal crack and structural evolution of the sample. Moreover, the digital volume correlation (DVC) method was also used to acquire the internal 3D strain field of the sample, and analyze the generation and development process of strain localization areas incurred by cracks.

2. Test Material and Test Methods

2.1. Test material and sample.

In this study, 1,3,5-triamino-2,4,6-trinitrobenzene (TATB)-based PBX was used as the test sample, and it was prepared into a cylindrical sample with size of *Φ5* mm × 5 mm. PBXs of this type are mainly constituted of PBX crystals and polymeric binder. The two materials present different gray values in CT images. In order to generate an ideal internal speckle field, the powder of a substitute material with mechanical properties similar to those of the above mentioned PBX was added during sample preparation.
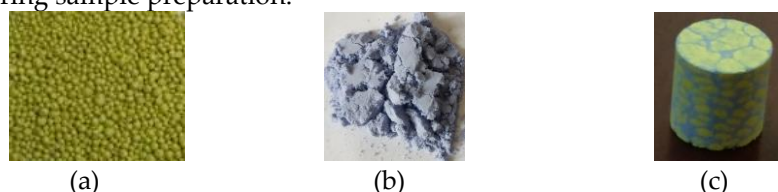

| (a) | (b) | (c) |

Fig. 1 Test sample   (a)Explosive graunles;(b) substitute material powder;(c) explosive grain

3.2. Compression test and in-situ computed tomography detection

The apparatus used for the in situ compression test is DEBEN (Microtest 5 kN) in situ stretch/compress experiment device. The sample is placed into the sample cabin of the loading device, as shown in Fig. 2. The compression process included a total of nine stages. After loading in each stage, the CT images of various stages were obtained through reconstruction. The axial loads were, respectively, 0 MPa, 1.99 MPa, 2.90 MPa, 3.97 MPa, 5.09 MPa, 6.01 MPa, 6.62 MPa, 7.23 MPa , 7.38 MPa, and 4.84 MPa (after peak). The sample is pressed with the compression rate of 0.2 mm min^{-1}.
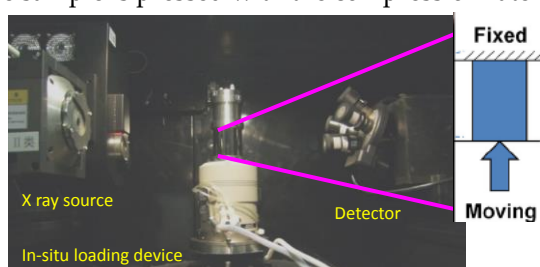

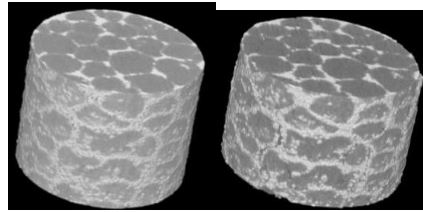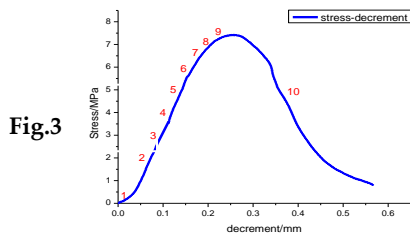**Fig. 2** Schematic illustration of CT scanning and in-situ loading

The CT scanning imaging experiments of the samples were carried out using a NanoVoxel device (Sanying Precision Engineering Research Center, Tianjin, China). The voltage and electric current of

the experiments were 100kV and 100μA, respectively. The sampling exposure time of monograph was 0.5ms. The number of projections was 900. The spatial resolution of the image obtained in this experiment was 13 μm pixel^{-1}.

4. Test Results and Analysis

4.1. Stress–decrement curve and computed tomography images

Fig. 3 was the stress–decrement curve of the sample. Fig. 4 provides the 3D reconstruction images of the sample at initial state and after failure, respectively. The outer surface of the sample reveals the existence of perforated cracks along the boundary of molding powder particles, and some cracks cut through molding powder particles and result in the crushing of these particles.

Fig.3

Fig.4

(a)   (b)

Fig. 3 Stress–decrement curve   **Fig.4** 3D reconstruction volumetric images.(a) Initial state; (b) after failure

Fig. 5 displays the CT images of the middle position (corresponding to section a position in Fig. 6a)) of the sample under different loads. Figs. 6 and 7, respectively, provide the images of the two longitudinal sections perpendicular to section a (section b and section c) shown by dashed lines under different loads. To be specific, the points with the highest gray value represent substitute material powder; that with the lowest gray value represents TATB crystals; and the gray value of binder falls between the gray value of substitute material and TATB. Limited by the resolution of the CT system, it was impossible to clearly observe the cracks until the axial load reached 7.23 MPa, as indicated by the cracks shown in Figs. 5c, 6c, and 7c. The cracks of the minimum scale clearly observable from CT images are referred to as CT scale cracks, and their width should be greater than one voxel. The crack distribution shown in Figs. 5d, 6d, and 7d demonstrates that the cracks mainly developed along the boundary of molding powder particles. When the strength of molding powder was relatively low and the angle of intersection between the long axis direction and the loading direction was too large, the energy required by cracks to cut through molding powder particles and propagate would be very low, indicating that they would cut through molding powder particles, propagate, and further crush these particles.
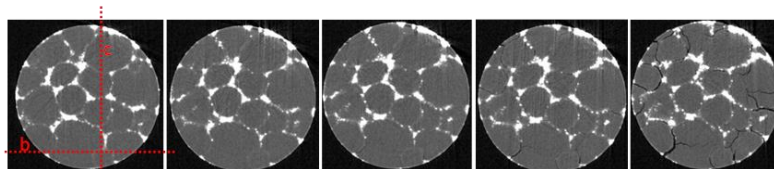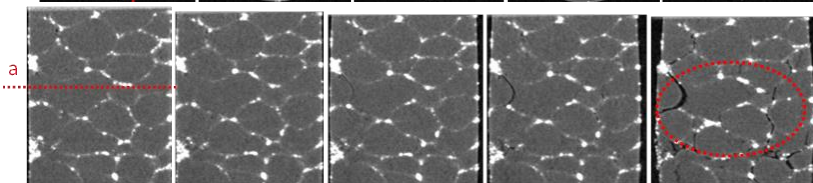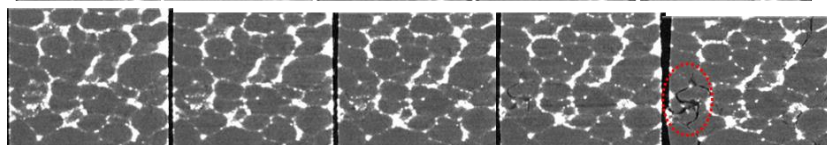
Fig.5

Fig.6

Fig.7

(a)   (b)   (c)   (d)   (e)

Fig. 5 CT images of the same transverse section (section a) under different load. **Fig. 6** CT images of the same longitudinal section (section b) under different loads. **Fig. 7** CT images of the same longitudinal section (section c) under different loads. (a)σ = 0 Mpa;(b)σ = 6.62 Mpa;(c)σ = 7.23 Mpa;(d)σ = 7.38 Mpa;(e)after peak

4.2. Displacement field calculation and analysis

Both the reference volume images and deformation volume images were segmented into subsets of an equal size (31×31×31 voxels, 403×403×403μm), respectively; and the interval between adjacent subsets was three voxels. Figs. 8, 9, and 10, respectively, provide the w displacement fields of section a (Fig. 5), v displacement fields of section b (Fig. 6), and u displacement fields of section c (Fig. 7) under the axial loads of 6.62, 7.23, and 7.38 MPa. Obvious deformation localization areas could already be observed in the areas enclosed by dashed lines in Figs. 10a and 11a. With the increase of load, these areas experienced further development and showed the existence of cracks; they corresponded respectively to the areas in which the cracks were located in Figs. 6e and 7e. In the gray image before sample failure, the gray values of these areas did not undergo any obvious variation, and the gray image failed to reflect the heterogeneity of the internal deformation of the sample.
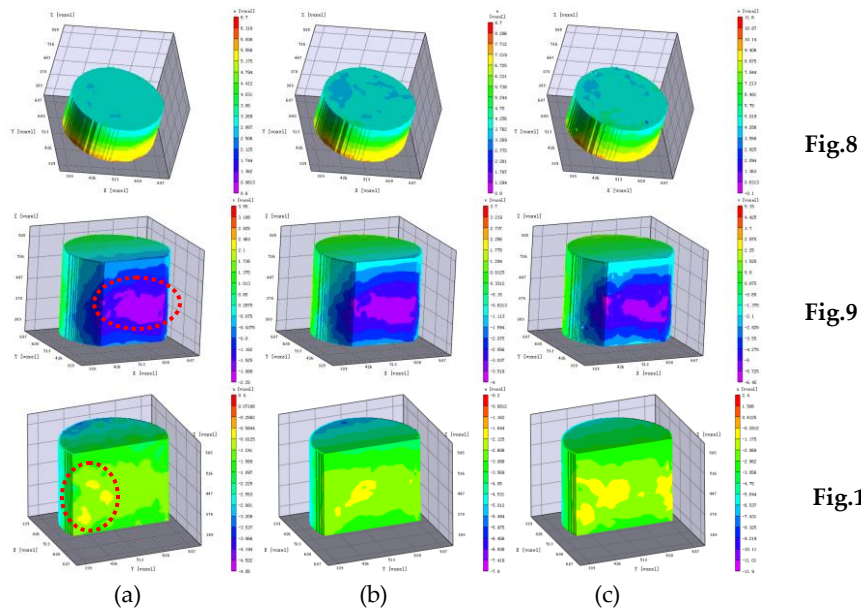

(a) (b) (c)

Fig. 8 u of section a. **Fig.9** v of section b. **Fig.10** w of section c.(a)σ = 6.62 MPa;(b)σ = 7.23 MPa; (c)σ = 7.38 MP

4.3. Strain field calculation and analysis

Figs. 11–13, respectively, provide the principal strain distribution maps of sections a, b, and c in three directions under the axial loads of 6.01, 6.62, 7.23, and 7.38 MPa. Strain field distribution can more clearly show the positions of the strain localization areas produced by cracks smaller than CT scale in the sample before the emergence of CT scale cracks, and thus reveal their development.

Under a relatively low load, the areas enclosed by dashed lines in Figs. 11–13 already show obvious strain localization areas, and several discrete high strain areas are mainly distributed at the boundary of particles and the edge of the sample. With the increase of load, these high strain areas experienced gradual development and coalescence, formed strain localization zones, and ultimately produced macro-cracks at localization zones. These areas corresponded, respectively, to the areas in which the cracks were located as shown in Figs. 5e, 6e, and 7e.

In order to reveal the internal deformation characteristics of the sample, $\varepsilon_v = \varepsilon_1 + \varepsilon_2 + \varepsilon_3$ can be used to calculate the volumetric strain. Fig. 14 provides the variations of the sample's total volumetric strain ε_v and mean of maximum principal strain with axial stress, and also the fitting curves of the two with axial stress. According to the volumetric strain curve, deformation was divided into three main stages. In stage AB, volumetric strain was negative, and the sample was compressed. At point B,

volumetric strain reached its minimum. In this stage, mean of maximum principal strain first experienced a rapid growth from zero, and then witnessed a slightly gentle growth trend. The initial micro-pores caused local strain concentration, and gave rise to the rapid growth of the principal strain. Furthermore, with the compression of the sample, some pores closed, sample deformation tended to be uniform, and the growth of mean of maximum principal strain also entered a relatively steady stage. With the continuous increase of load, the volumetric strain of the sample began to increase obviously. Point B was a point of inflection in the variations of volumetric strain, and could be defined as the initial point of dilatancy. The load corresponding to point B was 5.22 MPa, accounting for 72.5% of the peak load.
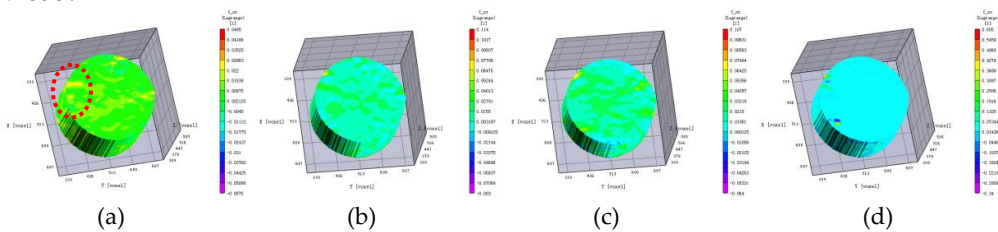

| (a) | (b) | (c) | (d) |

Fig. 11 ε_{xx} of section a. (a)σ = 6.62 MPa;(b)σ = 7.23 MPa;(c)σ = 7.38 MPa

| (a) | (b) | (c) | (d) |

Fig. 12 ε_{xx} strain field of section b. (a)σ = 6.62 MPa;(b)σ = 7.23 MPa;(c)σ = 7.38 MPa

| **(a)** | **(b)** | **(c)** | **(d)** |

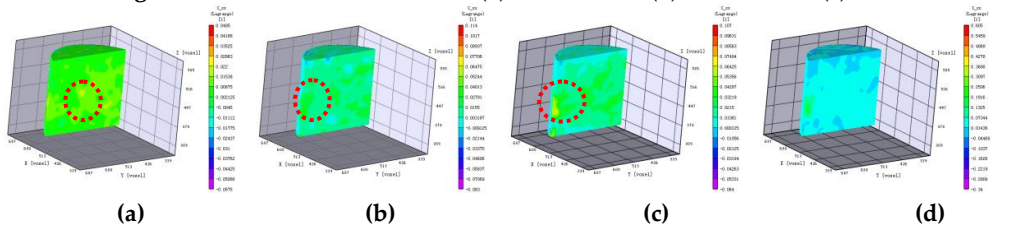**Fig. 13** ε_{xx} strain field of section c. (a)σ = 6.62 MPa;(b)σ = 7.23 MPa;(c)σ = 7.38 MPa

Stage BC mainly witnessed the development of micro-cracks smaller than CT scale, which resulted in the generation and propagation of local high strain areas. In this stage, mean of maximum principal strain grew at a faster pace. Local high strain areas emerged in Figs. 11(a), 12(a), and 13(a), and they later experienced further development. When load reached point C, the volumetric strain of the sample was zero. With the continuous increase of load, volumetric strain exceeded zero and grew rapidly; and the mean of maximum principal strain grew at a faster pace. The high strain areas shown in Figs. 11(c), 12(c), and 13(c) already gradually coalesced, and cracks could already be observed in Figs. 5(c), 6(c), and 7(c), indicating the development of micro-cracks into cracks larger than CT scale in this stage. These cracks ultimately formed macro-cracks perforating the sample, and resulted in complete sample failure. The axial stress corresponding to C was 6.91 MPa, accounting for 93% of the peak load. Point C served both as the initial point of the emergence of CT scale cracks inside the sample, and as the initial point of the occurrence of plastic deformation.
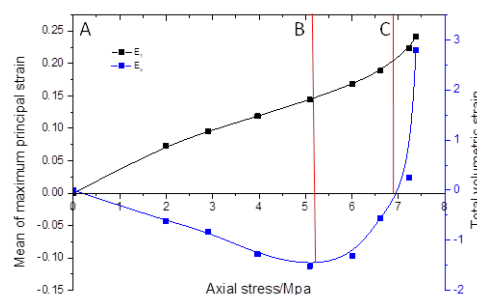

Fig. 14 Total volumetric strain, mean of maximum principal strain–Axial stress curves

5. Conclusions

(1) The boundary of molding powder particles was susceptible to failure and cracks. Owing to their relatively low strength, some molding powder particles were cut through and crushed by cracks.

(2) The displacement and strain distribution maps can directly display the heterogeneity of the internal deformation of PBXs in the compression process. Moreover, the strain field can reveal the generation and development process of the deformation localization areas incurred by micro-cracks smaller than CT scale at the boundary of molding powder particles.

(3) The deformation failure process of the sample was divided into three main stages. The initial points of both micro-cracks smaller than CT scale and CT scale cracks were defined as well. In this study, the development points of the cracks of two scales in the sample were, respectively, 72.5% and 93% of the peak stress, and they also corresponded to the initial point of dilatancy and the initial point of plastic deformation, respectively.

References

1. Belmas R, Reynier P. Mechanical behavior of pressed explosives[C]//International Symposium Energetic Materials Technology. Los Alamos:Los Alamos National Laboratory,1994:360-365.
2. Guo H，Luo J R，Shi P A，et al. Research on the fracture behavior of PBX under static tension[J]. Defence Technology, 2014,10(2):154-160.
3. Tao J, Wang X F, Zhao S X. The crack formation mechanism of an aluminized polymer bonded explosive under tension stress[J]. Journal of Energetic Materials,2017,35(2):172-178.
4. Zhou Z B, Chen P W, Huang F L, et al. Experimental study on the micromechanical behavior of a PBX stimulant using SEM and digital image correlation method[J]. Optics and Lasers in Engineering, 2011, 49:366-370.
5. Rae P J, Goldrein H T, Palmer S P J, et al. Quasi-static studies of the deformation and failure of β-HMX based polymer bonded explosives[J]. Proceedings of the Royal Society of London, Series A:Mathematical, Physical and Engineering Sciences, 2002, 458:743-762.
6. Li J L, Fu H, Tan D W. Fracture behavior investigation into a polymer-bonded explosive[J]. Strain, 2012, 48:463-473.
7. LI Jun-ling, FU Hua, TAN Duo-wang, et al. Fracture damage analysis of PBX[J]. Explosion and Shock Waves, 2011, 31(6):624-629.
8. Liu C, Thompson D G. Crack initiation and growth in PBX 9502 high explosive subject to compression[J]. Journal of Applied Mechanics, 2014, 81(10):1-13.
9. ZHOU Zhong-bin, CHEN Peng-wan, HUANG Feng-lei. An experimental study on the micro/macro fracture behavior of PBX using digital speckle correlation method[J]. Chinese Journal of High Pressure Physics, 2011, 25(1):1-7.
10. Rae P J, Palmer S P J, Goldrein H T, Lewis AL, Field J E. White-light digital image cross-correlation (DICC) analysis of the deformation of composite materials with random microstructure[J]. Optics and Lasers in Engineering, 2004, 41(4):635-648.
11. Li M, Zhang J, Xiong C Y. Fracture analysis of plastic bonded explosive by digital image correlation technique[C]//International Conference on Experimental Mechanics. Beijing: Proceeding of SPIE,2002, 4537:107-110.
12. Li M, Zhang J, Li J M, Wen M P. Experimental investigation to the damage localization of PBX mechanical failure at mesoscale[J]. Energetic Materials,2005,13(2):79-83.
13. Dai B, Lan L G, Zhang W B, Tian Yong. Study on the State of Internal Stress and Strain of TATB-based Polymer Bonded Explosive Using Strain Markers and Cone-Beam Computed Tomography[J]. Central European Journal of Energetic Materials , 2017,14 (3) :688-707.
14. Bay BK, Smith TS, Fyhie DP, et al. Digital volume correlation: Three-dimensional. Strain mapping using X-ray tomography[J]. Experimental Mechanics, 1999, 39(3): 217-226.